

Proposal for entangling gates on fluxonium qubits via a two-photon transition

Konstantin N. Nesterov,¹ Quentin Ficheux,² Vladimir E. Manucharyan,² and Maxim G. Vavilov¹

¹*Department of Physics and Wisconsin Quantum Institute,
University of Wisconsin-Madison, Madison, WI 53706, USA*

²*Department of Physics, Joint Quantum Institute, and Center for Nanophysics and
Advanced Materials, University of Maryland, College Park, MD 20742, USA*

(Dated: November 19, 2020)

We propose a family of microwave-activated entangling gates on two capacitively coupled fluxonium qubits. A microwave pulse applied to either qubit at a frequency near the half-frequency of the $|00\rangle - |11\rangle$ transition induces two-photon Rabi oscillations with a negligible leakage outside the computational subspace, owing to the strong anharmonicity of fluxoniums. By adjusting the drive frequency, amplitude, and duration, we obtain the gate family that is locally equivalent to the fermionic-simulation gates such as $\sqrt{\text{SWAP}}$ -like and controlled-phase gates. The gate error can be tuned below 10^{-4} for a pulse duration under 100 ns without excessive circuit parameter matching. Given that the fluxonium coherence time can exceed 1 ms, our gate scheme is promising for large-scale quantum processors.

I. INTRODUCTION

A programmable quantum computer requires very low error rate of the two-qubit gate operations, both for quantum error correction schemes to work [1, 2], and for extending the depth of quantum circuits during calculations on noisy intermediate-scale quantum processors [3]. In the superconducting circuits platform [4–6], major results were obtained using transmon qubits [7, 8], which are much closer to weakly anharmonic oscillators than to two-level systems. Although simplicity and robustness of transmons facilitated the creation of 25 – 100 qubit processors [9, 10], the weak anharmonicity and finite coherence time have been major factors limiting the gate errors. These challenges exist in both major families of two-qubit gates realized with these qubits: flux-tunable [11–16] and microwave-activated [17–23], where the gate speed is bounded by the anharmonicity.

Fluxonium qubits [24] are architecturally similar devices to transmons but they have a much stronger anharmonicity and considerably longer coherence times [25]. Theoretical proposals to realize two-qubit gates with fluxoniums and heavy fluxoniums have been previously based on driving transitions outside of computational subspace [26, 27]. A recent experiment demonstrated a fast two-qubit gate on fluxoniums activated by driving one of such transitions [28]. Because these noncomputational transitions generally have shorter lifetimes than the computational ones, such a gate scheme is exposed to additional error channels. In this work we consider a gate that keeps the state entirely in the computational subspace, hence benefiting in full from the long coherence of fluxonium qubits.

The entangling gate presented here is accomplished by a high-power microwave drive at half the frequency of the $|00\rangle - |11\rangle$ transition, which induces two-photon transitions between $|00\rangle$ and $|11\rangle$ and activates a coherent mixing in the $\{|00\rangle, |11\rangle\}$ subspace. With weak interaction in the computational subspace, the gate would normally be slow. However, the strong anharmonicity of fluxoniums

makes it possible to perform fast gate by increasing the drive amplitude without generating leakage to noncomputational levels. For realistic fluxonium parameters, we demonstrate that a 50 ns - long gate with $\pi/2$ mixing angle in the $\{|00\rangle, |11\rangle\}$ subspace can be realized with the leakage error below 10^{-4} and total gate error below 10^{-3} without using advanced pulse shaping. For longer gates, about 100 ns - long, the gate error can be reduced below 10^{-4} .

The entangling power and the local equivalence class of the proposed gates depend on the mixing angle in the $\{|00\rangle, |11\rangle\}$ subspace and on the magnitude of the effective ZZ coupling. The ZZ coupling originates from both the static level repulsion and an induced ac-Stark shift due to the large drive amplitude. This term modifies entangling properties of the gate. Interestingly, we show that for a half rotation in the $\{|00\rangle, |11\rangle\}$ subspace, the entangling power of the gate is independent of the contribution due to the total ZZ coupling. In fact, the family of gates with a half-rotation contains gates locally equivalent to $\sqrt{i\text{SWAP}}$ and $\sqrt{\text{SWAP}}$.

Entangling gates activated by two-photon processes were proposed and implemented in trapped-ion systems [29, 30]. In superconducting systems, a two-photon gate based on driving $|00\rangle - |11\rangle$ transition was demonstrated experimentally with transmon qubits [20]. This gate required frequency matching between $|0\rangle - |1\rangle$ transition of one transmon and $|1\rangle - |2\rangle$ transition of another transmon to increase the two-photon Rabi frequency by increasing the hybridization of $|11\rangle$ state with one of the noncomputational states. In case of fluxoniums, we can speed up the two-photon Rabi oscillations by increasing the drive amplitude. This trick does not cause leakage outside the computational subspace because of the strong anharmonicity of fluxoniums. Thus, the scheme presented here does not require frequency matching. In general, our gate benefits from higher frequencies of qubit transitions that lead to a stronger hybridization of states $|01\rangle$ and $|10\rangle$ and, therefore, a higher two-photon Rabi frequency. From practical considerations, the suggested

qubit frequency range is around 0.5 – 1 GHz.

While a single two-qubit gate combined with individual qubit controls is sufficient to generate a universal set of logical operations, some algorithms may compile more efficiently with a larger two-qubit gate set, especially if this set is hardware-efficient [31, 32]. For a given algorithm executed on a noisy processor, the maximal depth of a quantum circuit depends on a particular set of gates implemented on the hardware level. The gates based on mixing of $|00\rangle$ and $|11\rangle$ discussed here are locally equivalent to and can be easily mapped by single-qubit X rotations into the operations in the $\{|01\rangle, |10\rangle\}$ subspace. The family of the proposed gates is equivalent to a complete set of fSim gates for the fermionic-simulation problem [14, 33].

The outline of the paper is as follows. In Sec. II, we introduce our model and discuss relevant spectral properties of fluxonium circuits. In Sec. III, we consider coherent two-photon transitions between $|00\rangle$ and $|11\rangle$ two-qubit states and calculate their rate both analytically and numerically. In Sec. IV, we analyze two-qubit gates realized via the two-photon $|00\rangle - |11\rangle$ transition. We discuss local equivalence classes of such gates and their entangling power and simulate the gate error. We conclude in Sec. V.

II. CAPACITIVELY COUPLED FLUXONIUM QUBITS

The circuit diagram of two coupled fluxoniums, labeled as A and B , is shown schematically in Fig. 1(a). We model this system by the Hamiltonian

$$\hat{H} = \hat{H}_A^{(0)} + \hat{H}_B^{(0)} + \hat{V} + \hat{H}_{\text{drive}}, \quad (1)$$

where

$$\hat{H}_\alpha^{(0)} = 4E_{C,\alpha}\hat{n}_\alpha^2 + \frac{1}{2}E_{L,\alpha}\hat{\varphi}_\alpha^2 - E_{J,\alpha}\cos(\hat{\varphi}_\alpha - \phi_{\text{ext},\alpha}) \quad (2)$$

describes individual qubits ($\alpha = A, B$) [24]. The capacitive interaction between qubits is given by

$$\hat{V} = J_C\hat{n}_A\hat{n}_B, \quad (3)$$

and the coupling to an external microwave drive of frequency ω_d and phase γ_d – by

$$\hat{H}_{\text{drive}} = 2f(t)\cos(\omega_d t + \gamma_d)(\eta_A\hat{n}_A + \eta_B\hat{n}_B). \quad (4)$$

Here $f(t)$ is the time-dependent field envelope and η_A and η_B describe the coupling of each qubit to the driving field.

In these equations, the canonical variables are dimensionless flux $\hat{\varphi}_\alpha$ and charge (the number of Cooper pairs) \hat{n}_α , which satisfy the commutation relations $[\hat{\varphi}_\alpha, \hat{n}_{\alpha'}] = i\delta_{\alpha\alpha'}$. The kinetic-energy term in Eq. (2) is determined by the charging energy $E_{C,\alpha} = e^2/2C_\alpha$, where $(-e)$ is the electron charge and C_α is the total capacitance of the

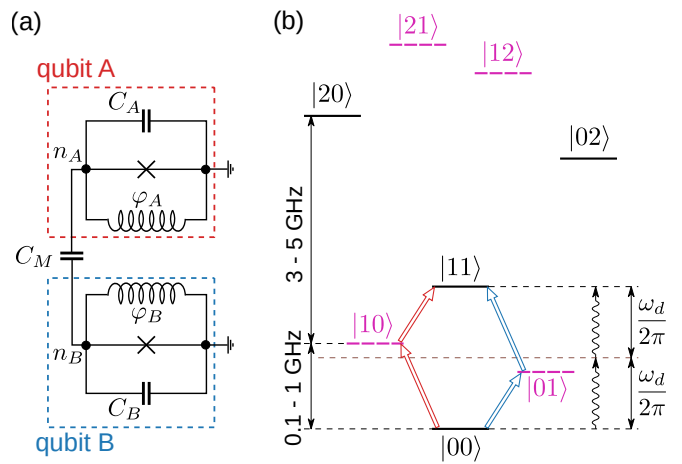


FIG. 1. (a) Circuit diagram of two capacitively coupled fluxonium qubits. (b) Energy levels (thick horizontal lines) of the coupled system are separated into two groups based on whether single-qubit indices have the same parity or not (black solid and magenta dashed lines). Transitions between different parity groups can be performed with a single microwave photon, while transitions within the same group require higher-order multiphoton processes. In the perturbative regime, the coherent two-photon transition between $|00\rangle$ and $|11\rangle$ is dominated by contributions from two virtual states generated by states $|10\rangle$ and $|01\rangle$ as shown by wide arrows. These contributions interfere destructively and exactly cancel each other when the coupling vanishes.

circuit α . The inductive energy is $E_{L,\alpha} = (\hbar/2e)^2/L_\alpha$, where $\hbar = h/2\pi$ is the reduced Planck constant and L_α is the effective linear inductance of a long chain of Josephson junctions, which is a hallmark of the fluxonium. This superinductance is shunted by a small junction, associated with the Josephson energy $E_{J,\alpha}$. The final term in Eq. (2) depends on $\phi_{\text{ext},\alpha} = (2e/\hbar)\Phi_{\text{ext},\alpha}$, where $\Phi_{\text{ext},\alpha}$ is the magnetic flux threading the loop formed by the small junction and superinductance. In the limit of $C_M \ll C_A, C_B$, the interaction strength in Eq. (3) is given by $J_C = 4e^2C_M/(C_A C_B)$ [26, 34].

Below, we assume that fluxonium circuits are at their half-flux-quantum sweet spots defined by $\phi_{\text{ext},\alpha} = \pi$, where the circuits are first-order insensitive to the external flux noise [35]. We label eigenstates of the Hamiltonian (2) as $|0_\alpha\rangle, |1_\alpha\rangle, |2_\alpha\rangle, \dots$ in the increasing order of the corresponding eigenenergies $E_0^\alpha \leq E_1^\alpha \leq \dots$. The first two levels of each circuit α form a qubit with transition frequency ω_{01}^α , where we define single-fluxonium frequencies as $\hbar\omega_{kl}^\alpha = E_l^\alpha - E_k^\alpha$. The qubit transition $|0_\alpha\rangle - |1_\alpha\rangle$ can display an exceptionally long coherence time exceeding $500 \mu\text{s}$ [25], which makes it an attractive choice for quantum-information storage. The qubit transition frequency $\omega_{01}^\alpha/2\pi$ is typically in the 100 MHz - 1 GHz range, which is much lower than conventional values in superconducting qubits. In addition, the charge matrix element n_{01}^α with the notation $n_{kl}^\alpha = |\langle k_\alpha | \hat{n}_\alpha | l_\alpha \rangle|$ is suppressed at low frequencies. At the same time, the transition $|1_\alpha\rangle - |2_\alpha\rangle$ has properties similar to those of the

transmon with a typical frequency of several GHz [35–37]. Because of the potential-energy symmetry at $\phi_{\text{ext},\alpha} = \pi$, the matrix elements of \hat{n}_α display parity selection rules, e.g., $n_{02}^\alpha = n_{13}^\alpha = 0$ [26, 36, 38]. However, n_{03}^α is not suppressed and can be of the order of n_{12}^α [36, 38].

We label interacting (dressed) two-qubit eigenstates of the Hamiltonian (1) at $\hat{H}_{\text{drive}} = 0$ as $|kl\rangle$ implying adiabatic connection to the noninteracting tensor-product states $|kl\rangle_0 = |k_A\rangle|l_B\rangle$. The frequency of the two-qubit transition $|kl\rangle - |k'l'\rangle$ is denoted as $\hbar\omega_{kl-k'l'} = E_{k'l'} - E_{kl}$, where E_{kl} is the eigenenergy of $|kl\rangle$. The two-qubit computational subspace $\{|00\rangle, |01\rangle, |10\rangle, |11\rangle\}$ is well separated from higher levels as illustrated schematically in Fig. 1(b). Two-qubit levels can be divided in two parity groups depending on whether $k+l$ is even or odd, which is shown by solid and dashed lines in Fig. 1(b). Because of the parity selection rules for the charge operators \hat{n}_A and \hat{n}_B , the interaction term (3) mixes levels within the same parity group only, while the matrix elements of the drive term (4) are nonzero only between levels belonging to different parity groups [26].

III. TWO-PHOTON TRANSITIONS

In this section, we consider a continuous drive of the two fluxoniums with a constant amplitude f in Eq. (4) and a drive frequency about half the frequency of the $|00\rangle - |11\rangle$ transition. Understanding this process is essential for the two-qubit gate discussed in Sec. IV.

A. Perturbative analysis

Even though two fluxonium excitations cannot be created by a single microwave photon, i.e., $\langle 00|\hat{H}_{\text{drive}}|11\rangle = 0$ because of the parity selection rules, the microwave drive can still induce the $|00\rangle - |11\rangle$ transition exchanging two fluxonium excitations with pairs of drive photons. The transition amplitude calculated to the leading (second) order in f can be understood as having contributions from cascaded sequential single-photon transitions via intermediate real states such as $|01\rangle$ and $|10\rangle$ and from coherent two-photon processes via intermediate virtual states [39]. Under certain conditions discussed below, the excitation probabilities of states $|01\rangle$ and $|10\rangle$ can remain low, while the system state oscillates between $|00\rangle$ and $|11\rangle$ with high visibility. Below, we apply a perturbation theory to estimate these probabilities and the frequency of the two-photon Rabi oscillations between $|00\rangle$ and $|11\rangle$. We approximate fluxoniums as two-level systems, which is reasonable given their strong anharmonicity.

The resonant Rabi frequency for a single-photon transition $|kl\rangle - |k'l'\rangle$ such as $|00\rangle - |10\rangle$ is given by the matrix elements of the drive, see Eq. (4):

$$\Omega_{kl-k'l'} = 2f|N_{kl,k'l'}|, \quad (5a)$$

where

$$N_{kl,k'l'} = \langle kl|(\eta_A\hat{n}_A + \eta_B\hat{n}_B)|k'l'\rangle. \quad (5b)$$

Without qubit interactions, the eigenstates of the system are product states of each qubit, $|kl\rangle_0 = |k_A\rangle \otimes |l_B\rangle$, and the Rabi frequencies (5a) reduce to the single-qubit Rabi frequencies for the $|0_\alpha\rangle - |1_\alpha\rangle$ transitions

$$\Omega_{\alpha,0} = 2f\eta_\alpha |\langle 1_\alpha|\hat{n}_\alpha|0_\alpha\rangle| \quad \{\alpha = A, B\}. \quad (6)$$

When driving with frequency $\omega_d = \bar{\omega}$, where

$$\bar{\omega} = \frac{\omega_{01}^A + \omega_{01}^B}{2}, \quad (7)$$

the upper bound on the probabilities P_α that the drive induces single-fluxonium transition can be estimated from the contrast of Rabi oscillations in two-level systems as

$$P_\alpha = \frac{\Omega_{\alpha,0}^2}{\Omega_{\alpha,0}^2 + (\Delta_{AB}/2)^2}, \quad (8)$$

where $\Delta_{AB} = |\omega_{01}^A - \omega_{01}^B|$ is the detuning between qubit frequencies. Taking $P_\alpha \ll 1$, we obtain conditions on the drive amplitudes,

$$\Omega_{\alpha,0} \ll \Delta_{AB}, \quad (9)$$

which combined with $\omega_d = \bar{\omega}$ imply that correlated two-qubit oscillations will dominate the dynamics of the system over independent single-qubit excitations.

We now consider the transition between $|00\rangle$ and $|11\rangle$, which is activated by two-photon processes when the drive frequency is $\bar{\omega}$. In this case, the system exhibits full oscillations of its probability being in one of the states, and the frequency $\tilde{\Omega}$ of such two-photon Rabi oscillations depends on the matrix element of the two-photon drive between $|00\rangle$ and $|11\rangle$. We apply the second-order perturbation theory together with the rotating-wave approximation (RWA) to obtain

$$\tilde{\Omega} = \frac{|\Omega_{00-01}\Omega_{01-11} - \Omega_{00-10}\Omega_{10-11}|}{\Delta_{AB}}, \quad (10)$$

This equation is reminiscent of a similar result derived for trapped ions excited with a bichromatic laser [29, 30]. By choosing $\omega_d = \bar{\omega}$ in the derivation of Eq. (10), we neglected the shift of the qubit frequencies due to the Stark shifts, which are quadratic in the drive amplitude f . Equation (10) describes destructive interference between the two contributions corresponding to two paths via virtual states generated by states $|01\rangle$ and $|10\rangle$, indicated by arrows in Fig. 1(b). Without interaction, $J_C = 0$, we observe that Rabi frequencies $\Omega_{kl-k'l'}$ for single-photon transitions reduce to single-qubit Rabi frequencies $\Omega_{A,0}$ and $\Omega_{B,0}$, and Eq. (10) yields $\tilde{\Omega} = 0$. This result emphasizes that entanglement is impossible without qubit interactions.

Let us now calculate the two-photon Rabi frequency to the first nonvanishing order in J_C . Correction to the

denominator of Eq. (10) is quadratic in J_C , while corrections to matrix elements are linear. Thus, we find that $\tilde{\Omega}$ is finite because of the hybridization of $|01\rangle$ with $|10\rangle$ and of $|00\rangle$ with $|11\rangle$. The interaction-dressed eigenstates in the first pair of states have the form

$$|01\rangle = |01\rangle_0 - \frac{J_{\text{eff}}}{\Delta_{AB}} |10\rangle_0, \quad |10\rangle = |10\rangle_0 + \frac{J_{\text{eff}}}{\Delta_{AB}} |01\rangle_0, \quad (11)$$

where $J_{\text{eff}} = J_C n_{01}^A n_{01}^B$. The mixing amplitude for the pair of states $|00\rangle$ and $|11\rangle$ has a form similar to Eq. (11), but with $2\bar{\omega}$ in the denominator instead of Δ_{AB} . Thus, the mixing of states $|00\rangle$ and $|11\rangle$ by interaction is reduced by $\Delta_{AB}/2\bar{\omega}$ compared to the one of states $|01\rangle$ and $|10\rangle$. This factor is not necessarily small in fluxonium qubits. Nevertheless, we ignore it for now to focus on the main principles. We find the following expression for the two-photon Rabi frequency:

$$\tilde{\Omega} = 2J_C n_{01}^A n_{01}^B \frac{\Omega_{A,0}^2 + \Omega_{B,0}^2}{\Delta_{AB}^2}. \quad (12)$$

The two-photon rate increases with hybridization in the computational subspace. One natural way to increase the latter is to reduce the detuning Δ_{AB} , which, however, enhances the magnitude of spurious single-photon excitations when driving at $\omega_d \approx \bar{\omega}$, see Eq. (8). To ensure the predominance of the two-photon process over single photon excitations, we fix the dimensionless amplitude $\Omega_{\alpha,0}/\Delta_{AB}$ rather than f since the dimensionless amplitude fully determines the relative importance of single-photon excitations, see Eq. (8). We conclude that reducing Δ_{AB} is not practical for increasing the rate of the two-photon $|00\rangle - |11\rangle$ transition. Equation (12) suggests that it is beneficial to have larger values of single-qubit charge matrix elements n_{01}^α . Because $n_{01}^\alpha = \omega_{01}^\alpha |\langle 0|\hat{\varphi}_\alpha|1\rangle_\alpha|/8E_{C,\alpha}$ [26], this condition means that having higher qubit frequencies is beneficial to make the two-photon Rabi oscillations faster.

In addition to inducing coherent two-photon oscillations, a strong drive at $\omega_d = \bar{\omega}$ induces ZZ interactions via the AC Stark effect (static ZZ interaction is absent in two-level models). In particular, we evaluate the relative phase accumulated in the computational subspace for a constant drive during time t :

$$\zeta = \frac{1}{\hbar} (\Delta E_{01} + \Delta E_{10} - \Delta E_{00} - \Delta E_{11}) t, \quad (13)$$

where ΔE_{kl} is the energy shift of level $|kl\rangle$ due to the AC Stark effect. Using the second order perturbation theory for the energy shifts due to the drive combined with the first order corrections in the coupling rate, Eq. (11), we find

$$\begin{aligned} \zeta &= \frac{\Omega_{00-10}^2 + \Omega_{10-11}^2 - \Omega_{00-01}^2 - \Omega_{01-11}^2}{\Delta_{AB}} t \\ &= \frac{4\Omega_{A,0}\Omega_{B,0}}{\Omega_{A,0}^2 + \Omega_{B,0}^2} \tilde{\Omega} t. \end{aligned} \quad (14)$$

In general, this phase accumulation is not negligible during a full Rabi period $t = 2\pi/\tilde{\Omega}$. Note that expression (14), obtained to the first order in interaction J_C , vanishes if the drive is applied to only one qubit.

A more rigorous analytic treatment of the two-photon process for fluxonium qubits is unnecessarily cumbersome. Below, we present a detailed numerical analysis of the two-photon Rabi oscillations in a system of two fluxoniums.

B. Numerical simulations of Rabi oscillations

Based on Eq. (12), we choose the single-qubit parameters for all numerical simulations in this paper as shown in Table I. With these values, both main qubit transition frequencies are relatively high compared to usual fluxonium qubits, which is accompanied by larger values of 0-1 charge matrix elements. In simulations, we first diagonalize Hamiltonians of single fluxonium circuits (2), and then work with the interacting system taking five lowest levels in each fluxonium. For simplicity, we only consider the case $\eta_A = \eta_B = 1$ here.

We plot the Rabi frequency for the $|00\rangle - |11\rangle$ transition as a function of the dimensionless drive amplitude

$$\lambda = \frac{\Omega_{A,0}}{\Delta_{AB}}, \quad (15)$$

see Fig. 2(a), and interaction strength J_C/h , see 2(b). Lines show calculations based on the analytic result (10) except that multi-level fluxonium qubits were used to compute energies and matrix elements, and symbols show results of numerical simulations, which were performed as follows. For given λ and J_C , we chose ω_d that maximizes the contrast between the minimum of $P_{00 \rightarrow 00}(t)$ and maximum of $P_{00 \rightarrow 11}(t)$, where $P_{kl \rightarrow k'l'}(t)$ is the population of state $|k'l'\rangle$ at time t for the initial state $|kl\rangle$ at $t = 0$. At each ω_d , we calculated these probabilities via time-domain simulations at time $t \geq 0$. In the drive term (4), we used a pulse with a Gaussian rising edge at $0 < t < t_{\text{rise}} = 25$ ns, which is given by

$$f(t) \propto \exp\left[-\frac{(t - t_{\text{rise}})^2}{2\sigma^2}\right] - \exp\left[-\frac{t_{\text{rise}}^2}{2\sigma^2}\right], \quad (16)$$

where $\sigma = t_{\text{rise}}/2$, and with the amplitude of the flat part ($t > t_{\text{rise}}$) determined by λ via Eq. (15). An example of such time-domain simulations of the occupation probabilities for ω_d that maximizes the contrast is shown in Fig. 2(c) for $\lambda = 0.5$ and $J_C/h = 300$ MHz. The optimal contrast in Fig. 2(c) is approximately 80%, which can be increased by increasing t_{rise} in Eq. (16). This contrast is at least 75% for all the pairs of λ and J_C discussed in Fig. 2 and is close to 100% for $\lambda \lesssim 0.1$. The observed period of oscillations in Fig. 2(c) is 147 ns, which corresponds to a Rabi frequency of 6.8 MHz in agreement with circles in Figs. 2(a) and (b). In a two-level system with qubit A parameters, $\lambda = 0.5$ corresponds to the 50%

	$E_{L,\alpha}/h$	$E_{C,\alpha}/h$	$E_{J,\alpha}/h$	$\omega_{01}^\alpha/2\pi$	$\omega_{12}^\alpha/2\pi$	$\omega_{23}^\alpha/2\pi$	$ \langle 0_\alpha \hat{n}_\alpha 1_\alpha \rangle $	$ \langle 1_\alpha \hat{n}_\alpha 2_\alpha \rangle $	$ \langle 0_\alpha \hat{n}_\alpha 3_\alpha \rangle $
qubit A	1.5 GHz	1.0 GHz	3.8 GHz	1.152 GHz	3.280 GHz	3.253 GHz	0.249	0.608	0.260
qubit B	0.9 GHz	1.0 GHz	3.0 GHz	0.849 GHz	2.929 GHz	2.683 GHz	0.207	0.567	0.277

TABLE I. Fluxonium parameters used for numerical simulations.

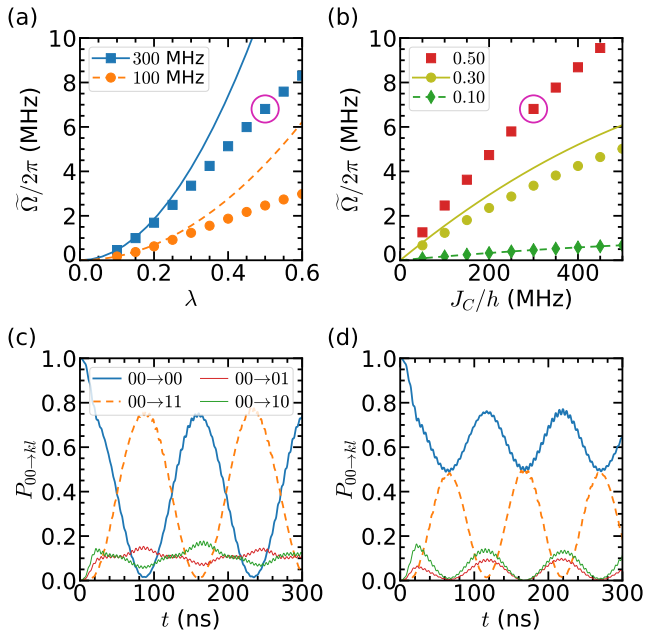


FIG. 2. (a), (b) Rabi frequency of the two-photon $|00\rangle - |11\rangle$ transition vs dimensionless drive amplitude λ [see Eq. (15)] at $J_C/h = 100$ and 300 MHz (a) and vs J_C/h at $\lambda = 0.1, 0.3$, and 0.5 (b). Lines show perturbative calculations using Eq. (10), and symbols show numerical simulations with the drive frequency ω_d chosen to maximize the contrast of Rabi oscillations. (c) Time evolution of computational-basis populations with the drive parameters corresponding to the circled data point in panel (a) and (b); the starting state is $|00\rangle$. (d) Same as in panel (c), but with a different ω_d , which yields oscillations that are approximately $\sqrt{2}$ faster than in panel (c).

contrast of single-photon Rabi oscillations, see Eq. (8), which agrees with appreciable occupations of states $|10\rangle$ and $|01\rangle$ in Fig. 2(c).

Both Figs. 2(a) and (b) demonstrate agreement between analytic and numerical calculations at $\lambda \lesssim 0.25$. We note that the perturbative result (10) was derived for two-level systems while Fig. 2 presents results for the full fluxonium Hamiltonian (2). Formal application of perturbation theory for a multi-level fluxonium yields additional terms in Eq. (10) generated by those higher energy noncomputational states $|kl\rangle$ ($k > 1$ or $l > 1$) that have nonzero values of $N_{00,kl}N_{kl,11}$, defined by Eq. (5b). They are exactly zero at $J_C = 0$ and acquire finite values at $J_C \neq 0$. If the rotating wave approximation (RWA) is used formally as the next step, such additional terms must be neglected in comparison to existing contribu-

tions because denominators of the new terms, which are determined by $\omega_{00-kl} - \bar{\omega}$, are much larger than denominators of existing contributions. However, formal application of the RWA is questionable in this case because possibly large values of n_{12}^α or n_{03}^α may make $N_{00,kl}N_{kl,11}$ to be sufficiently large and the corresponding additional contribution to Eq. (10) nonnegligible in comparison to the sum of existing terms, which interfere destructively. Equation (10) works for our choice of parameters when the higher energy states do not contribute significantly, but this approximation may be less accurate for other choices of fluxonium parameters, e.g., for qubits with larger $n_{12}^\alpha/n_{01}^\alpha$ or $n_{03}^\alpha/n_{01}^\alpha$.

At $\lambda \gtrsim 0.25$, the perturbation theory breaks down and the Rabi frequency increases slower than λ^2 . We emphasize that $\tilde{\Omega}$ still increases monotonically even far from the perturbative regime, when single-photon transitions can be strongly excited. It can become as large as a few MHz even for a relatively small J_C/h of 100 MHz and can surpass 10 MHz for stronger interaction strengths. We notice that $\tilde{\Omega}$ is close to be linear in J_C , which qualitatively agrees with Eq. (12). Accounting for hybridization between computational and higher energy states is necessary for a quantitative agreement.

The ability to induce two-photon Rabi oscillations can be used to realize an entangling gate involving the mixing of states $|00\rangle$ and $|11\rangle$ similar to bSWAP of Ref. [20]. A proper pulse shape is required to minimize single-photon transitions [e.g., $|00\rangle - |10\rangle$ in Fig. 2(c)] at the end of the pulse. In addition, driving the $|00\rangle - |11\rangle$ transition with a different ω_d creates off-resonant Rabi oscillations that exchange only a fraction of the population between states $|00\rangle$ and $|11\rangle$. In Fig. 2(d), ω_d is chosen to create oscillations of $\simeq 50\%$ of the state populations. Here, the minima of $P_{00 \rightarrow 01}(t)$ and $P_{00 \rightarrow 10}(t)$ occur at times where the state of the system is in an equal superposition of $|00\rangle$ and $|11\rangle$. This feature is not a generic property of our gate, but it results from our choice of values for the parameters λ and J_C . The resulting period of oscillations is 103 ns, which is approximately $\sqrt{2}$ shorter than 147 ns in Fig. 2(c). This behavior is reminiscent to that of a driven two-level system; the period of detuned Rabi oscillations with 50% contrast is exactly $\sqrt{2}$ times shorter than the period of resonant Rabi oscillations at fixed drive amplitude. It validates our understanding of the high-power drive of $|00\rangle - |11\rangle$ at $\bar{\omega}$ in a coupled-fluxonium system in terms of two-photon Rabi oscillations.

IV. ENTANGLING GATES

A. Theoretical concepts

We parametrize the family of gates spanned by the coherent mixing of $|00\rangle$ and $|11\rangle$ states and controlled-phase operations by two angles as

$$\hat{U}_{00-11}(\theta, \zeta) = \begin{pmatrix} \cos \frac{\theta}{2} & 0 & 0 & -i \sin \frac{\theta}{2} \\ 0 & e^{i\zeta/2} & 0 & 0 \\ 0 & 0 & e^{i\zeta/2} & 0 \\ -i \sin \frac{\theta}{2} & 0 & 0 & \cos \frac{\theta}{2} \end{pmatrix}. \quad (17)$$

In the absence of leakage outside of the computational subspace and provided that single-photon processes are negligible, any two-photon process described in the previous section can be reduced to the form (17) by means of single-qubit Z rotations applied from both sides of the operator, which can be implemented as virtual Z rotations in experiments [40].

In addition to the SWAP-like interaction – or $XX + YY$ interaction – described by θ in Eq. (17), the microwave drive create a ZZ interaction between computational states. This coupling leads to a finite ζ in Eq. (17), which cannot be changed to zero by local (single-qubit) operations. The ZZ term has two distinct contributions: the static ZZ coupling, which is caused by the repulsion between computational and noncomputational levels due to interaction (3), and the ZZ coupling induced by the microwave drive used to perform the gate. While the effect of the static ZZ coupling is relatively weak (the phase accumulation rate is slightly below 1 MHz for parameters of Table I with $J_C/h = 200$ MHz) and leads to a small contribution to $|\zeta| \ll \pi$ for short gate durations, the microwave-induced contribution to ζ can be large, as demonstrated in Eq. (14). Thus, one has to include the angle ζ in the definition of the target gate Eq. (17) to take into account this additional term caused by the drive. As we demonstrate below for three choices of the mixing angle θ , the value of ζ affects the equivalence class of the gate and its entangling properties.

1. Mixing angle $\theta = \pi$

First, we consider half a period of a resonant Rabi rotation, which corresponds to $\theta = \pi$ in Eq. (17). If $\zeta = 0$, the gate $U_{00-11}(\pi, 0)$ is bSWAP [20], which is a gate locally equivalent to iSWAP. On the other hand, $U_{00-11}(\pi, \pi)$ is locally equivalent to SWAP and thus does not generate entanglement.

In general, two gates $U_{00-11}(\pi, \zeta)$ having different values of ζ in the interval between 0 and π are not locally equivalent. Each class of locally equivalent gates is characterized by special invariants $G_1 = G'_1 + iG''_1$ and G_2 , and two gates are locally equivalent if and only if they have the same invariants [41, 42]. We calculate

them in Appendix A and find the following values for $U_{00-11}(\pi, \zeta)$:

$$G'_1 = -\sin^2 \frac{\zeta}{2}, \quad G''_1 = 0, \quad G_2 = \cos \zeta - 2. \quad (18)$$

Another important property of a two-qubit gate is the entangling power $\mathcal{P}(\theta, \zeta)$ [43, 44]. It ranges between $\mathcal{P} = 0$ for $\hat{U}_{00-11}(\pi, \pi)$ (equivalent to a SWAP gate), and $\mathcal{P} = 2/9$ for $\hat{U}_{00-11}(\pi, 0)$ (equivalent to an iSWAP gate). For arbitrary ζ , the entangling power is given by

$$\mathcal{P}(\theta = \pi, \zeta) = \frac{2}{9} \cos^2 \frac{\zeta}{2}, \quad (19)$$

see Appendix B.

2. Mixing angle $\theta = \pi/2$

When $\theta = \pi/2$, we also observe that the local equivalence class of $\hat{U}_{00-11}(\pi/2, \zeta)$ depends on ζ . For this mixing angle, the local equivalence classes are characterized by the invariants

$$G'_1 = \frac{\cos \zeta}{4}, \quad G''_1 = \frac{\sin \zeta}{4}, \quad G_2 = \cos \zeta. \quad (20)$$

For example, $\hat{U}_{00-11}(\pi/2, 0)$ is $\sqrt{\text{bSWAP}}$, which is locally equivalent to $\sqrt{\text{iSWAP}}$ [20], while $\hat{U}_{00-11}(\pi/2, \pi/2)$ and $\hat{U}_{00-11}(\pi/2, 3\pi/2)$ are equivalent to $(\sqrt{\text{SWAP}})^\dagger$ and $\sqrt{\text{SWAP}}$, respectively, which are not locally equivalent to each other and to $\sqrt{\text{iSWAP}}$.

The entangling power of $\hat{U}_{00-11}(\pi/2, \zeta)$ is independent of ζ and is equal to $\mathcal{P}(\theta = \pi/2, \zeta) = 1/6$. Thus, a gate in the $\theta = \pi/2$ family is guaranteed to be an entangling gate regardless of ζ . This is contrary to the case of $U_{00-11}(\theta = \pi, \zeta)$ gates, for which the entangling power varies according to Eq. (19).

The independence of the entangling power on values of ζ for $\theta = \pi/2$ makes this mixing angle attractive choice in situations when the induced ZZ coupling is hard to control. Another benefit of implementing a gate with $\theta = \pi/2$ vs a gate with $\theta = \pi$ is that the former gate can be realized with any off-resonant two-photon Rabi oscillations as long as their contrast $V = \max_t P_{00 \rightarrow 11}(t)$ is at least 0.5, while $\theta = \pi$ requires precise swapping of populations via half a period of a resonant Rabi rotation. For example, Fig. 2(d) demonstrates that it is possible to achieve $\theta = \pi/2$ by choosing half a period of the off-resonant Rabi oscillations with $V = 0.5$. The drive detuning from the two-photon resonance, $\omega_d = (E_{11} - E_{00})/2\hbar$, changes the contrast V and the period of Rabi oscillations, which, in turn, affects the gate duration and ζ in $\hat{U}_{00-11}(\pi/2, \zeta)$, see e.g. Eq. (14) for ζ at resonant drive frequency, when $V = 1$. Thus, the detuning acts as an additional control, which can be used either in the optimization procedure to improve gate performance when a specific ζ is not needed or in producing a gate with specific ζ .

We also note that $\hat{U}_{00-11}(\pi/2, \zeta)$ is sufficient to realize a gate given by the unitary (17) with any mixing angle θ by combining two gates $\hat{U}_{00-11}(\pi/2, \zeta)$ with single-qubit Z rotations. Some of those Z rotations can be substituted by a change of the microwave-drive phase γ_d in the drive term (4) for one of the two-qubit gates. More details are given in Appendix C. This decomposition is similar to the decomposition in Ref. [33] for XY gates, which are excitation-preserving swapping gates activating coherent rotations in the $\{|01\rangle, |10\rangle\}$ subspace. We note that $\hat{U}_{00-11}(\pi/2, \zeta)$ is not a Clifford gate for any ζ , which requires its characterization via the cross-entropy benchmarking [45] rather than via randomized benchmarking [46].

3. Mixing angle $\theta = 0$

We finally consider the case when $\theta = 0$. This gate occurs after a full two-photon Rabi oscillation with resonant, $\theta = \pi$, or off-resonant drive, e.g. $\theta = \pi/2$. The gate is equivalent to the controlled-phase gate with the invariants determined by ζ and coincide with invariants of the controlled-phase gate:

$$G'_1 = \cos^2 \frac{\zeta}{2}, \quad G''_1 = 0, \quad G_2 = \cos \zeta + 2. \quad (21)$$

The entangling power is also ζ -dependent:

$$\mathcal{P}(\theta = 0, \zeta) = \frac{2}{9} \sin^2 \frac{\zeta}{2}. \quad (22)$$

B. Simulated gate fidelity

Here we demonstrate via numerical simulations that a fast and high-fidelity gate that mixes states $|00\rangle$ and $|11\rangle$ by means of a monochromatic microwave drive is possible. We focus on the gate operation for the mixing angle $\theta = \pi/2$ and calculate the gate fidelity to an ideal unitary $\hat{U}(\pi/2, \zeta)$ with a suitable choice of ζ angle. As in Sec. III B, we perform simulations for qubit parameters shown in Table I and for fixed and equal drive couplings in Eq. (4), $\eta_A = \eta_B = 1$.

For a given gate duration t_{gate} , we use the Gaussian pulse shape with the rising edge given by Eq. (16), where $t_{\text{rise}} = t_{\text{gate}}/2$ and $\sigma = t_{\text{rise}}/2$. After solving the Schrödinger equation given by the time-dependent Hamiltonian (1) for four initial states in $\{|00\rangle, |01\rangle, |10\rangle, |11\rangle\}$, we obtain the propagator describing the evolution of computational states in a larger Hilbert space containing also higher energy levels. Projecting this operator into the computational subspace yields the simulated gate operator \hat{U}_{sim} . By adding single-qubit Z rotations before and after the gate, we adjust phases of relevant matrix elements of \hat{U}_{sim} to compare it with $\hat{U}_{00-11}(\pi/2, \zeta)$; more details are given in Appendix D. For the target unitary $\hat{U}_{00-11}(\pi/2, \zeta)$,

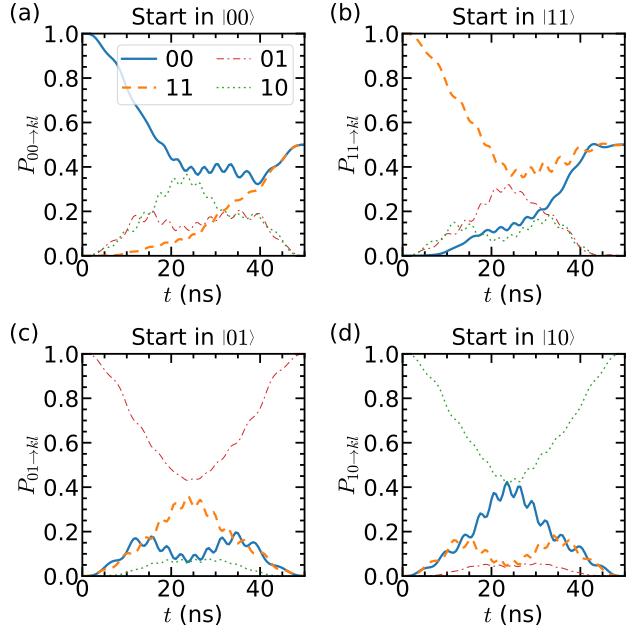


FIG. 3. Time evolution of the populations during the gate at $J_C/h = 200$ MHz for four initial computational states. The gate is optimized over the drive amplitude and frequency at fixed $t_{\text{gate}} = 50$ ns for the target operator $\hat{U}_{00-11}(\pi/2, \zeta)$. The gate fidelity is $F \approx 0.99905$ and $\zeta \approx 1.02\pi$.

we choose $\zeta = \varphi_{01,01} + \varphi_{10,10} - \varphi_{00,00} - \varphi_{11,11}$, where $\varphi_{kl,kl} = \arg\langle kl|\hat{U}_{\text{sim}}|kl\rangle$ is the diagonal-matrix-element phase of \hat{U}_{sim} , so a new value of ζ is chosen each time a new \hat{U}_{sim} is computed. Denoting the simulated gate operator after the application of Z rotations as \hat{U} , we use the standard expression for the two-qubit-gate fidelity [47]:

$$F = \frac{\text{Tr}(\hat{U}^\dagger \hat{U}) + \left| \text{Tr} \left[\hat{U}^\dagger \hat{U}_{00-11}(\pi/2, \zeta) \right] \right|^2}{20}. \quad (23)$$

Using this metric, we optimize the gate error over the drive frequency and amplitude. We analyze the dependence of F on the total gate duration t_{gate} and the interaction strength J_C .

As an example, we first illustrate the gate operation in time domain in Fig. 3 for such an optimized gate with $t_{\text{gate}} = 50$ ns and $J_C/h = 200$ MHz. We show transition probabilities $P_{kl \rightarrow k'l'}$ vs time for all 16 pairs of initial and final states formed from $\{|00\rangle, |01\rangle, |10\rangle, |11\rangle\}$. The simulated gate is found to be in the equivalence class determined by $\theta = \pi/2$ and $\zeta \approx 1.02\pi$ with the gate fidelity being $F \approx 0.99905$. The gate duration of $t_{\text{gate}} = 50$ ns is the shortest time for which $1 - F < 0.001$ for the interaction strength used in this simulation.

While the time evolution of state populations for the optimized gate of Fig. 3 exhibits multiple fluctuations and large transient excitations of one-photon processes, the gate performance is actually very robust to calibration errors. We illustrate this statement in Figs. 4(a) and

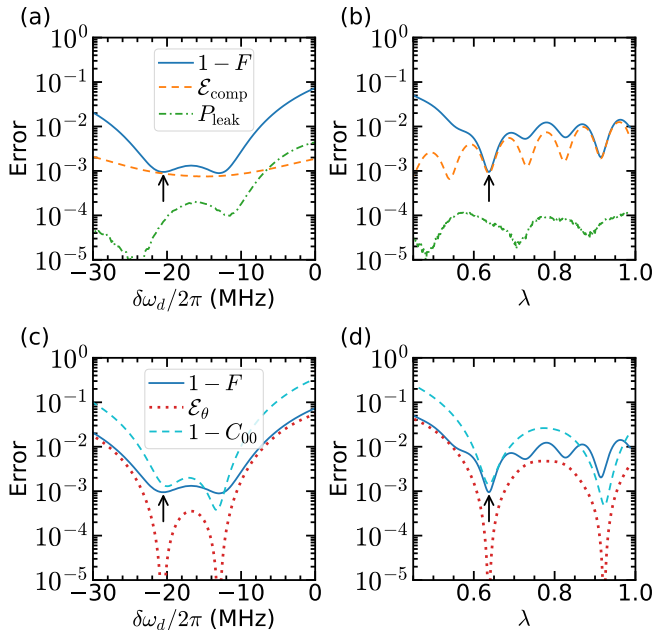


FIG. 4. Total gate error $1 - F$ (solid lines) and contributions to $1 - F$ vs $\delta\omega_d = \omega_d - \bar{\omega}$ at fixed λ (left panels) and vs λ at fixed ω_d (right panels) for the same parameters as in Fig. 3. The drive amplitude is the amplitude averaged over the pulse duration. The optimal values of $\delta\omega_d$ and λ , used in simulations of Fig. 3, are marked by vertical arrows. (a), (b) Contributions to $1 - F$ linear in population errors: the error due to incorrect populations of computational states $\mathcal{E}_{\text{comp}}$ (dashed line) and the average leakage probability to noncomputational states P_{leak} (dot-dashed line), see Eqs. (D5) and (D7). (c), (d) Mixing-angle error between $|00\rangle$ and $|11\rangle$ (dotted line), which is quadratic in the angle error, and concurrence error after the gate operation on $|00\rangle$ (dashed line), see Eqs. (D9) and (D10).

4(b), where we study gate properties around the optimal point by changing the drive frequency and amplitude. We notice that $1 - F$ is below 0.001 in the frequency interval greater than 1 MHz, see the solid line near the vertical arrow in Fig. 4(a). Longer gate duration can be chosen for which this interval is even wider.

We analyze various contributions to the gate error in Fig. 4 with more details given in Appendix D. For the ideal gate $\hat{U}_{00-11}(\pi/2, \zeta)$ operation, the transition probabilities $P_{kl \rightarrow k'l'}$ are either zero, 1/2, or 1, while the actual gate operation contains errors in those probabilities. When errors are small, $1 - F$ is well approximated by the sum of two distinct contributions that are linear in $P_{kl \rightarrow k'l'}$. The first contribution, $\mathcal{E}_{\text{comp}}$, is determined by those $P_{kl \rightarrow k'l'}$ for which $|k'l'\rangle$ is in the computational subspace, see Eq. (D5). The second contribution, P_{leak} , is the leakage error given by the average probability to end up outside of the computational subspace, see Eq. (D7). We show these two contribution by dashed and dash-dotted lines in Fig. 4(a) and 4(b). We find that at the optimal point, the gate error $1 - F$ is determined by

the error in the computational subspace $\mathcal{E}_{\text{comp}}$. Leakage errors are below 0.0001 at the optimal point. A more detailed analysis (not shown here) indicates that the remaining leakage errors are mostly coming from excitations of the second excited states of fluxonium circuits via, e.g., transitions $|10\rangle - |20\rangle$ and $|11\rangle - |12\rangle$.

While $\mathcal{E}_{\text{comp}}$ and P_{leak} are sufficient to explain the behavior of $1 - F$ near its minimum, other error mechanisms become dominant away from the optimal point. For instance, we find a large contribution from the mixing error \mathcal{E}_θ . This error is determined by the differences $|P_{00 \rightarrow 00} - P_{00 \rightarrow 11}|$ and $|P_{11 \rightarrow 00} - P_{11 \rightarrow 11}|$ and is quadratic in them. Essentially, it can be thought of as the error in the mixing angle θ in $\hat{U}_{00-11}(\theta, \zeta)$. We show this error by the dotted line in Figs. 4(c) and 4(d), which explains well the behavior of $1 - F$ far away from the optimal point.

In addition to the gate fidelity, we calculate the concurrence C_{00} (see Ref. [48]) of a state vector starting in $|00\rangle$ after the application of the gate, see Appendix D. It is shown by the dashed lines in Figs. 4(c) and 4(d). When $C_{00} = 1$, the state is maximally entangled and the gate is thus a perfect entangler. While the mixing error has two almost symmetric minima, which are sharp and deep, the two minima of the concurrence error are asymmetric. This is explained by the dependence of the concurrence not only on the mixing of states $|00\rangle$ and $|11\rangle$, but also on both amplitudes and phases of states $|01\rangle$ and $|10\rangle$, see Eq. (D10). The corresponding contributions coming from $|01\rangle$ and $|10\rangle$ have opposite signs in the left and right minima.

In Fig. 5, we show gate error and its budget as a function of gate duration t_{gate} and the interaction strength J_C . For $J_C/h = 200$ MHz, we observe that the coherent error can easily go below 10^{-4} for a gate duration shorter than 100 ns. In bottom panels, we show parameter ζ that determines the equivalence class of the gate. Its tendency to decrease with increasing t_{gate} or J_C is explained by the contribution to ζ coming from the static ZZ coupling. The effect of static ZZ grows with the gate duration and interaction strength. Finally we notice that combining two $\hat{U}_{00-11}(\pi/2, \zeta)$ gates, we can obtain a controlled-phase gate with phase 2ζ .

V. DISCUSSION AND CONCLUSIONS

We demonstrated that fast high-fidelity two-qubit gates are possible in fluxonium circuits when the system state remains entirely in the low-energy computational subspace. Despite a relatively weak effect of capacitive interaction between fluxoniums on the computational subspace, the gate time can still be as short as 50 ns due to the strong anharmonicity of the fluxonium spectrum. The anharmonicity typically limits the intensity of the microwave drive. We demonstrated that the microwave amplitude could be large for the proposed two-photon gate without causing noticeable leakage of the state outside of the computational subspace during

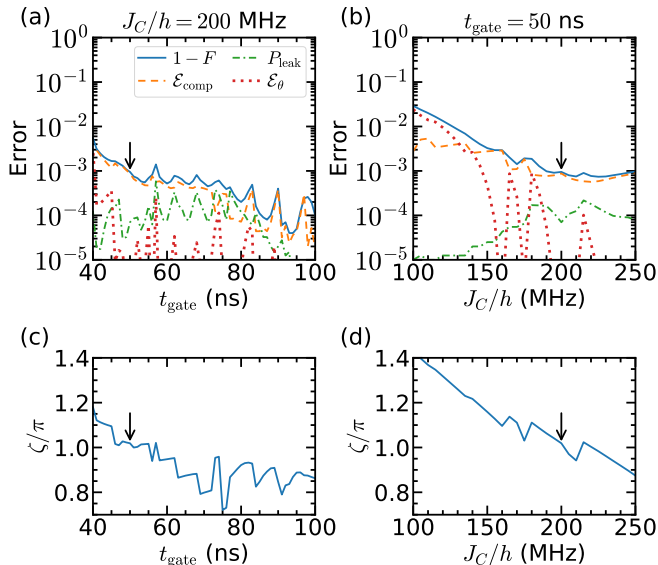


FIG. 5. (a), (b) Optimized gate error and error budget vs total gate duration t_{gate} at $J_C/h = 200$ MHz (a) and vs J_C/h at $t_{\text{gate}} = 50$ ns (b). Line styles follow the convention of Fig. 4. (c), (d) Parameter ζ determining the local-equivalence class [see Eq. (17)] of the same optimized gates as in the corresponding top panels. Vertical arrows in all four panels indicate parameters of Fig. 3.

the pulse, minimizing the effect of decoherence on the gate fidelity.

At a weak drive power, the rate of two-photon transitions is quadratic in the drive amplitude. In this case, the gate would be prohibitively long if the drive were chosen so that single-photon transitions between subspaces $\{|00\rangle, |11\rangle\}$ and $\{|01\rangle, |10\rangle\}$ were strongly suppressed. We demonstrated that unintended single-photon transitions between those subspaces could be reduced even for a strong drive by fine-tuning the pulse amplitude and frequency together with gate duration. As a result, the microwave pulse only mixes states $|00\rangle$ and $|11\rangle$. We focused on the half-mixing angle $\theta = \pi/2$ for which the entangling power is independent of the phase shift due to the ZZ interaction, which guarantees that the gate is entangling without any control of the Stark-induced phase accumulation. We also note that the half-mixing gate is shorter and is often more robust to pulse imperfections.

ACKNOWLEDGMENTS

We would like to thank Mark Dykman, Ivan Pechenezhskiy, and Long Nguyen for fruitful discussions. We acknowledge the support from NSF PFC at JQI and ARO-LPS HiPS program (grant No. W911NF-18-1-0146). V.E.M. and M.G.V acknowledge the Faculty Research Award from Google and fruitful conversations with the members of the Google Quantum AI team.

We used the QuTiP software package [49, 50] and performed computations using resources and assistance of the UW-Madison Center For High Throughput Computing (CHTC) in the Department of Computer Sciences. The CHTC is supported by UW-Madison, the Advanced Computing Initiative, the Wisconsin Alumni Research Foundation, the Wisconsin Institutes for Discovery, and the National Science Foundation.

Appendix A: Local invariants

Here we calculate the invariants [41, 42] for the gates described by Eq. (17) and demonstrate that the Stark shift ζ makes the gates with different ζ nonequivalent to each other.

To calculate the local invariants, we express the gate operator in the Bell basis defined by the transformation operator

$$Q = \frac{1}{\sqrt{2}} \begin{pmatrix} 1 & 0 & 0 & i \\ 0 & i & 1 & 0 \\ 0 & i & -1 & 0 \\ 1 & 0 & 0 & -i \end{pmatrix}.$$

We define $U_B = Q^\dagger U_{00-11}(\theta, \zeta) Q$ and $m(U_{00-11}) = U_B^T U_B$. The local invariants [42] are given by:

$$G_1 = \frac{\text{tr}^2[m(U)]}{16 \det U} = \frac{e^{-i\zeta}}{4} (e^{i\zeta} + \cos \theta)^2 \quad (\text{A1a})$$

and

$$G_2 = \frac{\text{tr}^2[m(U)] - \text{tr}[m^2(U)]}{4 \det U} = (2 \cos \theta + \cos \zeta), \quad (\text{A1b})$$

where $G_1 = G'_1 + iG''_1$ is a complex number and G_2 is real. We obtain G_1 and G_2 for arbitrary ζ and two choices of $\theta = \pi/2$ and π , presented by Eqs. (18) and (20).

Appendix B: Entangling power

Here we provide expressions for calculations of the entangling power \mathcal{P} of a two-qubit operator (17) [43]. We use the algebraic technique of Ref. [44] that defines the entangling power as

$$\mathcal{P}(U) = \frac{4}{9} [E(U) + E(US_{12}) - E(S_{12})], \quad (\text{B1})$$

where $E(U)$ is the operator entanglement (linear entropy) of U :

$$E(U) = 1 - \frac{1}{16} \text{Tr} [U^R (U^R)^\dagger U^R (U^R)^\dagger],$$

the matrix U^R is obtained from U by realignment:

$$(U^R)_{ij,kl} = U_{ik,jl},$$

and S_{12} is the swapping operator

$$S_{12} = \sum_{ij} |ij\rangle\langle ji| = \begin{pmatrix} 1 & 0 & 0 & 0 \\ 0 & 0 & 1 & 0 \\ 0 & 1 & 0 & 0 \\ 0 & 0 & 0 & 1 \end{pmatrix}.$$

We take $U(\theta, \zeta)$ in the form of Eq. (17) and find

$$\mathcal{P}(\theta, \zeta) = \frac{1}{36} (5 - 4 \cos \zeta \cos \theta - \cos 2\theta). \quad (\text{B2})$$

We notice that only for $\theta = \pi/2$ the entangling power is independent of the Stark shift ζ .

Appendix C: Gates decomposition

Here we show how an operation $\hat{U}_{00-11}(\theta, \zeta)$, which is given by Eq. (17), can be decomposed into two operations $\hat{U}_{00-11}(\pi/2, \zeta/2)$ and single-qubit Z rotations. This decomposition has the form

$$\begin{aligned} \hat{U}_{00-11}(\theta, \zeta) &= \hat{U}_Z \left(-\frac{\theta}{2} \right) \hat{U}'_{00-11} \left(\frac{\pi}{2}, \frac{\zeta}{2}, \theta - \frac{\pi}{2} \right) \\ &\times \hat{U}'_{00-11} \left(\frac{\pi}{2}, \frac{\zeta}{2}, -\theta + \frac{\pi}{2} \right) \hat{U}_Z \left(-\frac{\theta}{2} \right), \end{aligned} \quad (\text{C1})$$

where

$$\hat{U}_Z(\nu) = \hat{Z}_\nu^A \otimes \hat{Z}_\nu^B = \text{diag} (e^{-i\nu}, 1, 1, e^{i\nu}) \quad (\text{C2})$$

is the tensor product of two single-qubit Z rotations $\hat{Z}_\nu = \text{diag} (e^{-i\nu/2}, e^{i\nu/2})$ of qubits A and B and

$$\hat{U}'_{00-11} \left(\frac{\pi}{2}, \frac{\zeta}{2}, \gamma \right) = \hat{U}_Z \left(\frac{\gamma}{2} \right) \hat{U}_{00-11} \left(\frac{\pi}{2}, \frac{\zeta}{2} \right) \hat{U}_Z \left(-\frac{\gamma}{2} \right). \quad (\text{C3})$$

The last gate operation differs from $\hat{U}_{00-11}(\pi/2, \zeta/2)$ by having additional phase factors $e^{i\gamma}$ and $e^{-i\gamma}$ in the off-diagonal matrix elements of the $\{|00\rangle, |11\rangle\}$ subspace. In addition to performing Z rotations as in Eq. (C3), this can be achieved by adjusting the microwave-drive phase γ_d in Eq. (4): a change $\delta\gamma_d$ in that phase results in the change of $2\delta\gamma_d$ in γ [20]. Essentially, this is equivalent to virtual Z rotations, which amount to a change of the reference frame by changing phases of microwave pulses [40]. The decomposition (C1) is reminiscent of a similar decomposition in Ref. [33] for XY gates, which are swapping gates in the $\{|01\rangle, |10\rangle\}$ subspace.

Appendix D: Gate fidelity and error budget

In the ideal gate operation $\hat{U}_{00-11}(\pi/2, \zeta)$ with $\pi/2$ mixing angle, transition probabilities $P_{kl \rightarrow k'l'}$ are either 0, 1, or 1/2. Here we assume small deviations $\epsilon_{k'l',kl}$ from such values and calculate their contribution to the gate error. By using single-qubit Z rotations from both sides, we can write a realistic gate operator projected into the computational subspace as

$$\hat{U}_{\text{real}} = \begin{pmatrix} \sqrt{\frac{1}{2} - \epsilon_{00,00}} & \sqrt{\epsilon_{00,01}} e^{i\varphi_{00,01}} & \sqrt{\epsilon_{00,10}} e^{i\varphi_{00,10}} & \sqrt{\frac{1}{2} - \epsilon_{00,11}} (-ie^{i\beta/2}) \\ \sqrt{\epsilon_{01,00}} e^{i\varphi_{01,00}} & \sqrt{1 - \epsilon_{01,01}} e^{i\zeta/2} & \sqrt{\epsilon_{01,10}} e^{i\varphi_{01,10}} & \sqrt{\epsilon_{01,11}} e^{i\varphi_{01,11}} \\ \sqrt{\epsilon_{10,00}} e^{i\varphi_{10,00}} & \sqrt{\epsilon_{10,01}} e^{i\varphi_{10,01}} & \sqrt{1 - \epsilon_{10,10}} e^{i\zeta/2} & \sqrt{\epsilon_{10,11}} e^{i\varphi_{10,11}} \\ \sqrt{\frac{1}{2} - \epsilon_{11,00}} (-ie^{i\beta/2}) & \sqrt{\epsilon_{11,01}} e^{i\varphi_{11,01}} & \sqrt{\epsilon_{11,10}} e^{i\varphi_{11,10}} & \sqrt{\frac{1}{2} - \epsilon_{11,11}} \end{pmatrix}. \quad (\text{D1})$$

Because of the possible leakage to noncomputational levels, which we also describe by the same errors $\epsilon_{k'l',kl}$, this projected operator is generally nonunitary. The unitarity of the operator before the projection into the computational subspace implies that

$$\epsilon_{00,kl} + \epsilon_{11,kl} = \sum_{k'l' \notin \{00,11\}} \epsilon_{k'l',kl} \quad (\text{D2})$$

for $kl \in \{00, 11\}$ and

$$\epsilon_{kl,kl} = \sum_{k'l' \neq kl} \epsilon_{k'l',kl} \quad (\text{D3})$$

for $kl \in \{01, 10\}$, where the sum in the r.h.s. of Eq. (D3) includes noncomputational states. Because of the probability errors, Eq. (D1) also contains an additional phase

factor $e^{i\beta/2}$ in the off-diagonal matrix element. Because of the unitarity of the operator before the projection, the value of β is not constant and we find that it is at least linear in probability errors, $\beta = O(\epsilon)$.

To the linear order in the population errors $\epsilon_{k'l',kl}$, we obtain the fidelity of the real gate (D1) [47]

$$\begin{aligned} F &= \frac{\text{Tr} \left(\hat{U}_{\text{real}}^\dagger \hat{U}_{\text{real}} \right) + \left| \hat{U}_{\text{real}}^\dagger \hat{U}_{00-11}(\pi/2, \zeta) \right|^2}{20} \\ &= 1 - \mathcal{E}_{\text{comp}} - P_{\text{leak}} + O(\epsilon^2). \end{aligned} \quad (\text{D4})$$

Here

$$\mathcal{E}_{\text{comp}} = \frac{1}{5} (\epsilon_{00}^{\text{comp}} + \epsilon_{01}^{\text{comp}} + \epsilon_{10}^{\text{comp}} + \epsilon_{11}^{\text{comp}}) \quad (\text{D5})$$

is the error due to leakage to wrong computational levels, where

$$\epsilon_{kl}^{\text{comp}} = \begin{cases} \epsilon_{01,kl} + \epsilon_{10,kl} & \text{if } kl \in \{00, 11\} \\ \epsilon_{00,kl} + \epsilon_{11,kl} + \epsilon_{lk,kl} & \text{if } kl \in \{01, 10\} \end{cases} \quad (\text{D6})$$

is the probability to leak to the wrong computational state if starting in state $|kl\rangle$. The second contribution in Eq. (D4) is the error due to the leakage to noncomputational levels, which is given by

$$P_{\text{leak}} = 1 - \frac{1}{4} \text{Tr} \left(\hat{U}_{\text{real}}^\dagger \hat{U}_{\text{real}} \right) = \frac{1}{4} (\epsilon_{00}^{\text{leak}} + \epsilon_{01}^{\text{leak}} + \epsilon_{10}^{\text{leak}} + \epsilon_{11}^{\text{leak}}), \quad (\text{D7})$$

where

$$\epsilon_{kl}^{\text{leak}} = \begin{cases} \epsilon_{00,kl} + \epsilon_{11,kl} - \epsilon_{kl}^{\text{comp}} & \text{if } kl \in \{00, 11\} \\ \epsilon_{kl,kl} - \epsilon_{kl}^{\text{comp}} & \text{if } kl \in \{01, 10\} \end{cases} \quad (\text{D8})$$

is the probability to leak to higher states if starting in the computational state $|kl\rangle$.

Apparently, linear leakage is insufficient to explain all the errors away from optimal point. There, we need to consider another source of error that is quadratic in ϵ :

$$\mathcal{E}_\theta = \frac{(\epsilon_{00,00} - \epsilon_{11,00})^2 + (\epsilon_{00,11} - \epsilon_{11,11})^2}{20} \quad (\text{D9})$$

This is the error in the mixture of $|00\rangle$ and $|11\rangle$ states in the Bell state.

We also calculate concurrence for the starting state $|00\rangle$ using the realistic gate operator (D1). To this end, we first find the component of the final state in the computational subspace $|\psi(t_{\text{gate}})\rangle = \hat{U}_{\text{real}}|00\rangle$. We calculate $|\tilde{\psi}(t_{\text{gate}})\rangle = \hat{\sigma}_y \otimes \hat{\sigma}_y |\psi^*(t_{\text{gate}})\rangle$ and find the concurrence [48]

$$C_{00} = \left| \langle \tilde{\psi} | \psi \rangle \right| = \left| \sqrt{(1 - 2\epsilon_{00,00})(1 - 2\epsilon_{11,00})} + 2i\sqrt{\epsilon_{01,00}\epsilon_{10,00}}e^{i(\varphi_{01,00} + \varphi_{10,00} - \beta/2)} \right|. \quad (\text{D10})$$

For $\epsilon_{01,00} = 0$, we have $1 - C_{00} \simeq (\epsilon_{00,00} + \epsilon_{11,00})$.

-
- [1] S. B. Bravyi and A. Yu. Kitaev, “Quantum codes on a lattice with boundary,” arXiv:quant-ph/9811052 (1998).
- [2] A. G. Fowler, M. Mariantoni, J. M. Martinis, and A. N. Cleland, “Surface codes: Towards practical large-scale quantum computation,” *Phys. Rev. A* **86**, 032324 (2012).
- [3] J. Preskill, “Quantum Computing in the NISQ era and beyond,” *Quantum* **2**, 79 (2018).
- [4] M. H. Devoret and R. J. Schoelkopf, “Superconducting Circuits for Quantum Information: An Outlook,” *Science* **339**, 1169 (2013).
- [5] G. Wendin, “Quantum information processing with superconducting circuits: a review,” *Rep. Prog. Phys* **80**, 106001 (2017).
- [6] M. Kjaergaard, M. E. Schwartz, J. Braumüller, P. Krantz, J. I-J Wang, S. Gustavsson, and W. D. Oliver, “Superconducting Qubits: Current State of Play,” *Annu. Rev. Condens. Matter Phys* **11**, 369 (2020).
- [7] A. Blais, R.-S. Huang, A. Wallraff, S. M. Girvin, and R. J. Schoelkopf, “Cavity quantum electrodynamics for superconducting electrical circuits: An architecture for quantum computation,” *Phys. Rev. A* **69**, 062320 (2004).
- [8] J. Koch, T. M. Yu, J. Gambetta, A. A. Houck, D. I. Schuster, J. Majer, A. Blais, M. H. Devoret, S. M. Girvin, and R. J. Schoelkopf, “Charge-insensitive qubit design derived from the Cooper pair box,” *Phys. Rev. A* **76**, 042319 (2007).
- [9] F. Arute, K. Arya, R. Babbush, D. Bacon, J. C. Bardin, R. Barends, R. Biswas, S. Boixo, F. G. S. L. Brandao, D. A. Buell, B. Burkett, Y. Chen, Z. Chen, B. Chiaro, R. Collins, W. Courtney, A. Dunsworth, E. Farhi, B. Foxen, A. Fowler, C. Gidney, M. Giustina, R. Graff, K. Guerin, S. Habegger, M. P. Harrigan, M. J. Hartmann, A. Ho, M. Hoffmann, T. Huang, T. S. Humble, S. V. Isakov, E. Jeffrey, Z. Jiang, D. Kafri, K. Kechedzhi, J. Kelly, P. V. Klimov, S. Knysh, A. Korotkov, F. Kostritsa, D. Landhuis, M. Lindmark, E. Lucero, D. Lyakh, S. Mandrà, J. R. McClean, M. Mcewen, A. Megrant, X. Mi, K. Michielsen, M. Mohseni, J. Mutus, O. Naaman, M. Neeley, C. Neill, M. Y. Niu, E. Ostby, A. Petukhov, J. C. Platt, C. Quintana, E. G. Rieffel, P. Roushan, N. C. Rubin, D. Sank, K. J. Satzinger, V. Smelyanskiy, K. J. Sung, M. D. Trevithick, A. Vainsencher, B. Villalonga, T. White, Z. J. Yao, P. Yeh, A. Zalcman, H. Neven, and J. M. Martinis, “Quantum supremacy using a programmable superconducting processor,” *Nature* **574**, 505 (2019).
- [10] P. Jurcevic, A. Javadi-Abhari, L. S. Bishop, I. Lauer, D. F. Bogorin, M. Brink, L. Capelluto, O. Günliük, T. Itoko, N. Kanazawa, A. Kandala, G. A. Keefe, K. Kruslich, W. Landers, E. P. Lewandowski, D. T. McClure, G. Nannicini, A. Narasgond, H. M. Nayfeh, E. Pritchett, M. B. Rothwell, S. Srinivasan, N. Sundaresan, C. Wang, K. X. Wei, C. J. Wood, J.-B. Yau, E. J. Zhang, O. E. Dial, J. M. Chow, and J. M. Gambetta, “Demonstration of quantum volume 64 on a superconducting quantum computing system,” arXiv:2008.08571 (2020).
- [11] R. Barends, J. Kelly, A. Megrant, A. Veitia, D. Sank, E. Jeffrey, T. C. White, J. Mutus, A. G. Fowler, B. Campbell, Y. Chen, Z. Chen, B. Chiaro, A. Dunsworth, C. Neill, P. O’malley, P. Roushan, A. Vainsencher, J. Wenner, A. N. Korotkov, A. N. Cleland, and J. M. Martinis, “Superconducting quantum circuits at the surface code threshold for fault tolerance,” *Nature* **508**, 500 (2014).
- [12] Yu Chen, C. Neill, P. Roushan, N. Leung, M. Fang, R. Barends, J. Kelly, B. Campbell, Z. Chen, B. Chiaro,

- A Dunsworth, E Jeffrey, A Megrant, J Y Mutus, P J J O'Malley, C M Quintana, D Sank, A Vainsencher, J Wenner, T C White, Michael R Geller, A N Cleland, and John M Martinis, "Qubit Architecture with High Coherence and Fast Tunable Coupling," *Phys. Rev. Lett.* **113**, 220502 (2014).
- [13] M. C. Collodo, J. Herrmann, N. Lacroix, C. K. Andersen, A. Remm, S. Lazar, J.-C. Besse, T. Walter, A. Wallraff, and C. Eichler, "Implementation of Conditional-Phase Gates based on tunable ZZ-Interactions," arXiv:2005.08863 (2020).
- [14] B. Foxen, C. Neill, A. Dunsworth, P. Roushan, B. Chiaro, A. Megrant, J. Kelly, Z. Chen, K. Satzinger, R. Barends, F. Arute, K. Arya, R. Babbush, D. Bacon, J. C. Bardin, S. Boixo, D. Buell, B. Burkett, Yu Chen, R. Collins, E. Farhi, A. Fowler, C. Gidney, M. Giustina, R. Graff, M. Harrigan, T. Huang, S. V. Isakov, E. Jeffrey, Z. Jiang, D. Kafri, K. Kechedzhi, P. Klimov, A. Korotkov, F. Kostritsa, D. Landhuis, E. Lucero, J. McClean, M. Mcewen, X. Mi, M. Mohseni, J. Y. Mutus, O. Naaman, M. Neeley, M. Niu, A. Petukhov, C. Quintana, N. Rubin, D. Sank, V. Smelyanskiy, A. Vainsencher, T. C. White, Z. Yao, P. Yeh, A. Zalcman, H. Neven, and J. M. Martinis, "Demonstrating a Continuous Set of Two-qubit Gates for Near-term Quantum Algorithms," arXiv:2001.08343 (2020).
- [15] V. Negrneac, H. Ali, N. Muthusubramanian, F. Battistel, R. Sagastizabal, M. S. Moreira, J. F. Marques, W. Vlothuizen, M. Beekman, N. Haider, A. Bruno, and L. Dicarlo, "High-fidelity controlled-Z gate with maximal intermediate leakage operating at the speed limit in a superconducting quantum processor," arXiv:2008.07411 (2020).
- [16] Y. Sung, L. Ding, J. Braumüller, A. Vepsäläinen, B. Kannan, M. Kjaergaard, A. Greene, G. O. Samach, C. McNally, D. Kim, A. Melville, B. M. Niedzielski, M. E. Schwartz, J. L. Yoder, T. P. Orlando, S. Gustavsson, and W. D. Oliver, "Realization of high-fidelity CZ and ZZ-free iSWAP gates with a tunable coupler," arXiv:2011.01261 (2020).
- [17] P. J. Leek, S. Filipp, P. Maurer, M. Baur, R. Bianchetti, J. M. Fink, M. Göppl, L. Steffen, and A. Wallraff, "Using sideband transitions for two-qubit operations in superconducting circuits," *Phys. Rev. B* **79**, 180511 (2009).
- [18] J. M. Chow, A. D. Córcoles, Jay M Gambetta, Chad Rigetti, B R Johnson, John A Smolin, J R Rozen, George A Keefe, Mary B Rothwell, Mark B Ketchen, and M Steffen, "Simple All-Microwave Entangling Gate for Fixed-Frequency Superconducting Qubits," *Phys. Rev. Lett.* **107**, 080502 (2011).
- [19] J. M. Chow, J. M. Gambetta, A. D. Córcoles, S. T. Merkel, J. A. Smolin, C. Rigetti, S. Poletto, G. A. Keefe, M. B. Rothwell, J. R. Rozen, M. B. Ketchen, and M. Steffen, "Universal Quantum Gate Set Approaching Fault-Tolerant Thresholds with Superconducting Qubits," *Phys. Rev. Lett.* **109**, 060501 (2012).
- [20] S. Poletto, J. M. Gambetta, S. T. Merkel, J. A. Smolin, J. M. Chow, A. D. Córcoles, G. A. Keefe, M. B. Rothwell, J. R. Rozen, D. W. Abraham, C. Rigetti, and M. Steffen, "Entanglement of Two Superconducting Qubits in a Waveguide Cavity via Monochromatic Two-Photon Excitation," *Phys. Rev. Lett.* **109**, 240505 (2012).
- [21] Jerry M. Chow, Jay M. Gambetta, Andrew W. Cross, Seth T. Merkel, Chad Rigetti, and M. Steffen, "Microwave-activated conditional-phase gate for superconducting qubits," *New J. Phys.* **15**, 115012 (2013).
- [22] Sarah Sheldon, Easwar Magesan, Jerry M Chow, and Jay M Gambetta, "Procedure for systematically tuning up cross-talk in the cross-resonance gate," *Phys. Rev. A* **93**, 60302 (2016).
- [23] S. Krinner, P. Kurpiers, B. Royer, P. Magnard, I. Tsitsilin, J.-C. Besse, A. Remm, A. Blais, and A. Wallraff, "Demonstration of an All-Microwave Controlled-Phase Gate between Far-Detuned Qubits," *Phys. Rev. Applied* **14**, 044039 (2020).
- [24] V. E. Manucharyan, J. Koch, L. I. Glazman, and M. H. Devoret, "Fluxonium: Single Cooper-Pair Circuit Free of Charge Offsets," *Science* **326**, 113–116 (2009).
- [25] L. B. Nguyen, Y.-H. Lin, A. Somoroff, R. Mencia, N. Grabon, and V. E. Manucharyan, "High-Coherence Fluxonium Qubit," *Phys. Rev. X* **9**, 041041 (2019).
- [26] K. N. Nesterov, I. V. Pechenezhskiy, C. Wang, V. E. Manucharyan, and M. G. Vavilov, "Microwave-activated controlled-Z gate for fixed-frequency fluxonium qubits," *Phys. Rev. A* **98**, 030301 (2018).
- [27] M. Abdelhafez, B. Baker, A. Gyenis, P. Mundada, A. A. Houck, D. Schuster, and J. Koch, "Universal gates for protected superconducting qubits using optimal control," *Phys. Rev. A* **101**, 022321 (2020).
- [28] Q. Ficheux, L. B. Nguyen, A. Somoroff, H. Xiong, K. N. Nesterov, M. G. Vavilov, and V. E. Manucharyan, "Fast logic with slow qubits: microwave-activated controlled-Z gate on low-frequency fluxoniums," arXiv:2011.02634 (2020).
- [29] A. Sørensen and K. Mølmer, "Entanglement and quantum computation with ions in thermal motion," *Phys. Rev. A* **62**, 022311 (2000).
- [30] J. Benhelm, G. Kirchmair, C. F. Roos, and R. Blatt, "Towards fault-tolerant quantum computing with trapped ions," *Nature Physics* **4**, 463–466 (2008).
- [31] I. D. Kivlichan, J. McClean, N. Wiebe, C. Gidney, A. Aspuru-Guzik, G. K.-L. Chan, and R. Babbush, "Quantum Simulation of Electronic Structure with Linear Depth and Connectivity," *Phys. Rev. Lett.* **120**, 110501 (2018).
- [32] N. Lacroix, C. Hellings, C. K. Andersen, A. Di Paolo, A. Remm, S. Lazar, S. Krinner, G. J. Norris, M. Gabureac, J. Heinsoo, A. Blais, C. Eichler, and A. Wallraff, "Improving the Performance of Deep Quantum Optimization Algorithms with Continuous Gate Sets," *Phys. Rev. X Quantum* **1**, 110304 (2020).
- [33] D. M. Abrams, N. Didier, B. R. Johnson, M. P. Da Silva, and C. A. Ryan, "Implementation of the XY interaction family with calibration of a single pulse," arXiv:1912.04424 (2019).
- [34] Uri Vool and Michel Devoret, "Introduction to quantum electromagnetic circuits," *Int. J. Circ. Theor. Appl.* **45**, 897–934 (2017).
- [35] Vladimir E Manucharyan, Nicholas A Masluk, Archana Kamal, Jens Koch, Leonid I Glazman, and Michel H Devoret, "Evidence for coherent quantum phase slips across a Josephson junction array," *Phys. Rev. B* **85**, 24521 (2012).
- [36] Guanyu Zhu and Jens Koch, "Asymptotic expressions for charge-matrix elements of the fluxonium circuit," *Phys. Rev. B* **87**, 144518 (2013).
- [37] Yen-Hsiang Lin, Long B Nguyen, Nicholas Grabon, Jonathan San Miguel, Natalia Pankratova, and

- Vladimir E Manucharyan, “Demonstration of Protection of a Superconducting Qubit from Energy Decay,” *Phys. Rev. Lett.* **120**, 150503 (2018).
- [38] Guanyu Zhu, David G Ferguson, Vladimir E Manucharyan, and Jens Koch, “Circuit QED with fluxonium qubits: Theory of the dispersive regime,” *Phys. Rev. B* **87**, 24510 (2013).
- [39] C. J. Foot, *Atomic Physics* (Oxford University Press, New York, 2005).
- [40] D. C. McKay, C. J. Wood, S. Sheldon, J. M. Chow, and J. M. Gambetta, “Efficient Z gates for quantum computing,” *Phys. Rev. A* **96**, 022330 (2017).
- [41] Yu. Makhlin, “Nonlocal Properties of Two-Qubit Gates and Mixed States, and the Optimization of Quantum Computations,” *Quantum Inf. Process.* **1**, 243 (2002).
- [42] J. Zhang, J. Vala, S. Sastry, and K. B. Whaley, “Geometric theory of nonlocal two-qubit operations,” *Phys. Rev. A* **67**, 042313 (2003).
- [43] P. Zanardi, C. Zalka, and L. Faoro, “Entangling power of quantum evolutions,” *Phys. Rev. A* **62**, 030301 (2000).
- [44] Z. Ma and X. Wang, “Matrix realignment and partial-transpose approach to entangling power of quantum evolutions,” *Phys. Rev. A* **75**, 014304 (2007).
- [45] S. Boixo, S. V. Isakov, V. N. Smelyanskiy, R. Babbush, N. Ding, Z. Jiang, M. J. Bremner, J. M. Martinis, and H. Neven, “Characterizing quantum supremacy in near-term devices,” *Nature Physics* **14**, 595 (2018).
- [46] E. Magesan, J. M. Gambetta, B. R. Johnson, C. A. Ryan, J. M. Chow, S. T. Merkel, M. P. Da Silva, G. A. Keefe, M. B. Rothwell, T. A. Ohki, M. B. Ketchen, and M. Steffen, “Efficient Measurement of Quantum Gate Error by Interleaved Randomized Benchmarking,” *Phys. Rev. Lett.* **109**, 080505 (2012).
- [47] Line Hjørtshøj Pedersen, Niels Martin Møller, and Klaus Mølmer, “Fidelity of quantum operations,” *Phys. Lett. A* **367**, 47–51 (2007).
- [48] W. K. Wootters, “Entanglement of Formation of an Arbitrary State of Two Qubits,” *Phys. Rev. Lett.* **80**, 2245 (1998).
- [49] J. R. Johansson, P. D. Nation, and F. Nori, “QuTiP: An open-source Python framework for the dynamics of open quantum systems,” *Comp. Phys. Comm.* **183**, 1760 (2012).
- [50] J. R. Johansson, P. D. Nation, and F. Nori, “QuTiP 2: A Python framework for the dynamics of open quantum systems,” *Comp. Phys. Comm.* **184**, 1234 (2013).